Available online at www.sciencedirect.com
ScienceDirect
C. R. Mecanique 335 (2007) 269–279
COMPTES RENDUS MECANIQUE
http://france.elsevier.com/direct/CRAS2B/

Melting and solidification: processes and models/Flows in solidification

3D macrosegregation simulation with anisotropic remeshing

Sylvain Gouttebroze [a], Michel Bellet [a], Hervé Combeau [b,*]

[a] *CEMEF, École des mines de Paris, BP207, 06904 Sophia Antipolis cedex, France*
[b] *LSG2M, Écoles des mines de Nancy, parc de Saurupt, 54000 Nancy, France*

Abstract

The article presents a three-dimensional coupled numerical solution of momentum, mass, energy and solute conservation equations, for binary alloy solidification. The interdendritic flow in the mushy zone is assumed to obey the Darcy's law. Microsegregation is governed by the lever rule, assuming local equilibrium at phase interfaces. The resulting energy and solute advection–diffusion equations are solved using the Streamline-Upwind/Petrov–Galerkin (SUPG) finite element method. A SUPG-PSPG velocity-pressure formulation is applied for the momentum equation. The full algorithm was implemented in the 3D code THERCAST, together with an anisotropic remeshing method. Two applications have been considered: a small ingot of Pb-48wt%Sn alloy and a large steel ingot. The numerical results of these two cases are presented with the evolution of temperature, liquid velocity, and solute concentration fields during solidification. ***To cite this article: S. Gouttebroze et al., C. R. Mecanique 335 (2007).***

Résumé

Simulation 3D de la macroségrégation avec remaillage anisotrope. Un modèle numérique de simulation des transferts couplés de chaleur, de masse et de quantité de mouvement pendant la solification d'un alliage binaire est présenté. Les équations du modèle sont classiques, l'écoulement du liquide interdendritrique est décrit par une loi de type Darcy. Le modèle des bras de levier (équilibre complet entre les phases liquide et solide) a été adopté pour la microsgégrégation. Le modèle numérique a été élaboré suivant la méthode des éléments finis pour des géométries tri-dimensionnelles dans le code THERCAST. Les équations de conservation de l'énergie et de la masse de soluté ont été discrétisées à l'aide d'un schéma SUPG et celles de la quantité de mouvement et de la masse totale par un schéma SUPG-PSPG. L'originalité de ce travail provient de la mise en oeuvre d'une méthode de maillage évolutif qui permet d'obtenir une bonne précision de calcul avec un nombre d'éléments de calcul raisonnable. Deux applications illustratives sont présentées, une première application concerne le cas d'un petit domaine pour un alliage Pb-48wt%Sn et la deuxième, un lingot d'acier. ***Pour citer cet article : S. Gouttebroze et al., C. R. Mecanique 335 (2007).***

Keywords: Computational fluid mechanics; Solidification; Macrosegregation; Finite element; Remeshing

Mots-clés : Mécanique des fluides numérique ; Solidification ; Macroségrégation ; Eléments finis ; Remaillage

* Corresponding author.
E-mail addresses: sylvain.gouttebroze@sintef.no (S. Gouttebroze), Herve.Combeau@mines.u-nancy.fr (H. Combeau).

1631-0721/$ – see front matter
doi:10.1016/j.crme.2007.05.005

1. Introduction

Solidification of alloys generates the segregation of solutes (chemical species) at the scale of the microstructure, called microsegregation. This inhomogeneity can be redistributed by any driving force promoting a relative velocity between the solid and the liquid phases; this is called macrosegregation. Only the natural thermal and solutal convection of the liquid phase has been considered in this work, the solid phase being considered as fixed. Macrosegregation can affect mechanical and chemical properties and so its prediction is essential to optimize cast products. This phenomenon is particularly important in the solidification of large ingots. However, most three-dimensional simulations are currently made on small ingots or pieces of about 10 centimeters high [1,2]. This is due to the fact that the flow field is more complex and unstable in larger casting, and that a good accuracy in the prediction of macrosegregation requires a fine mesh in the mushy zone. In order to overcome such difficulties, the main idea of the present contribution relies on the implementation of an adaptive remeshing technique. This strategy allows a good accuracy combined with an optimal computational effort particularly for large ingot simulation.

The equations of the macrosegregation model and the strategy adopted in THERCAST, a three-dimensional finite element solidification code developed by CEMEF [3] are presented in the first part. Then, the remeshing method is described. Finally, the capabilities of the method are illustrated on two cases: a small ingot reproducing the conditions of the Hebditch–Hunt experiment for a Pb-48wt%Sn alloy and a large steel ingot of 2 m height with a pseudo-2D approach.

2. Conservation equations and discretization

The conservation equations for mass, momentum, solute and energy constitute the core of a macrosegregation model. These equations can be derived from three main approaches: volumetric averaging techniques [4], continuum model of mixture theory [5], and stochastic averaging [6]. This last method has been used for this work. We refer to [7] for a discussion on the range of validity of the different assumptions of the model. The conservation equations are recalled and their finite element discretization is presented.

2.1. Conservation of mass and momentum

The main hypotheses of the mechanical model are the following:

- rigid and fixed solid phase;
- the liquid is Newtonian, the viscosity constant and the flow laminar;
- solid and liquid phase densities are equal ($\rho = \rho_s = \rho_l$) and constant ($\rho = \rho_0$), except in the buoyancy term ($\tilde{\rho} g$) according to the Boussinesq approximation. The density of the liquid phase depends on the temperature T and the solute content in the liquid phase c_l:

$$\tilde{\rho} = \rho_0\big[1 - \beta_T (T - T_{\text{ref}}) - \beta_c (c_l - c_l^{\text{ref}})\big] \tag{1}$$

  where β_T and β_c are the thermal and solutal expansion coefficients respectively, and ρ_0 is the density in the liquid assumed constant. T_{ref} is the reference temperature imposed equal to the liquidus temperature at the initial solute concentration in the liquid, c_l^{ref};
- a saturated mixture, i.e.:

$$g_s + g_l = 1 \tag{2}$$

  where g_s and g_l are the solid and liquid volumetric fraction respectively;
- the mushy region is modelled as an isotropic porous medium whose permeability, K, is defined by the Carman–Kozeny formula:

$$K = \frac{\lambda_2^2 g_l^3}{180(1 - g_l)^2} \tag{3}$$

One can notice that λ_2 in Eq. (3) corresponds to a characteristic size of the microstructure in the mushy zone, which is generally estimated as an average secondary dendrite arm spacing. More complex models of permeability [8] are

available in the literature and could be easily implemented in the model. The choice of this permeability law has been done mainly for comparison reasons with previous results (from Refs. [1] and [14]).

Due to the fact that the densities of the solid and liquid phases are equal and constant, notably shrinkage is neglected, the mass conservation equation is reduced to:

$$\nabla \cdot \mathbf{V} = 0 \tag{4}$$

where $\mathbf{V}$ is the so-called mixture velocity. According to Eq. (2) we have: $\mathbf{V} = g_l \mathbf{V_l} + g_s \mathbf{V_s} = g_l \mathbf{V_l}$.

As presented in a previous paper [9], the classical mixture theory [5] yields to the following momentum conservation equation:

$$\rho_0 \frac{\mathrm{d}\mathbf{V}}{\mathrm{d}t} = \nabla \cdot (\mu \nabla \mathbf{V}) - \nabla P + \tilde{\rho} g - \frac{\mu}{K} \mathbf{V} \tag{5}$$

where $\mathbf{V}$ and P are the unknown velocity and pressure fields, and μ is the dynamic viscosity of the liquid.

A SUPG-PSPG formulation has been used to discretise the momentum equation together with the mass conservation equation. The SUPG-PSPG formulation, presented for CFD finite element calculations by Tezduyar et al. [10], is based on three stabilization coefficients: a τ_{SUPG} coefficient (Streamline-Upwind/Petrov–Galerkin), a τ_{PSPG} coefficient (Pressure-Stabilizing/Petrov–Galerkin) and a τ_{LSIC} coefficient (least-squares on incompressibility constraint) as presented in Eq. (6).

$$\begin{aligned}
&\int_{\Omega} \left(\rho_0 \frac{\partial \mathbf{V}}{\partial t} + \rho_0 \nabla \cdot (\mathbf{V} \times \mathbf{V}) - \nabla \cdot (\mu \nabla \mathbf{V}) + \frac{\mu}{K} \mathbf{V} - \tilde{\rho} g \right) \cdot \mathbf{V}^* \, \mathrm{d}\Omega + \int_{\Omega} P^* \nabla \cdot \mathbf{V} \, \mathrm{d}\Omega \\
&\quad + \sum_{e=1}^{n_{\mathrm{elt}}} \int_{\Omega_e} \left(\rho_0 \frac{\partial \mathbf{V}}{\partial t} + \rho_0 \nabla \cdot (\mathbf{V} \times \mathbf{V}) - \nabla \cdot (\mu \nabla \mathbf{V}) + \frac{\mu}{K} \mathbf{V} - \tilde{\rho} g \right) \cdot \frac{1}{\rho_0} (\tau_{\mathrm{SUPG}} \rho_0 \mathbf{V} \cdot \nabla \mathbf{V}^* + \tau_{\mathrm{PSPG}} \nabla P^*) \, \mathrm{d}\Omega \\
&\quad + \sum_{e=1}^{n_{\mathrm{elt}}} \int_{\Omega_e} \tau_{\mathrm{LSIC}} \nabla \cdot \mathbf{V}^* \rho_0 \nabla \cdot \mathbf{V} \, \mathrm{d}\Omega = 0
\end{aligned} \tag{6}$$

where $\mathbf{V}^*$ and P^* are the test functions of the finite elements for the velocity and pressure fields respectively. The stabilisation coefficients (τ_{SUPG}, τ_{PSPG} and τ_{LSIC}) depend on the local mesh size, which is calculated in the flow direction. As this isotropic stabilisation is applied on anisotropic mesh, the accuracy of the solution might be affected. However, in the remeshing strategy, presented in the next section, the stretching of the elements is limited and so is the possible inaccuracy.

2.2. Energy conservation equation

Using the above hypotheses, the energy balance can be written in the form:

$$\frac{\partial H}{\partial t} + \mathbf{V} \cdot \nabla (\rho c_p T) - \nabla \cdot (k \nabla T) = 0 \tag{7}$$

Assuming that the specific heat c_p is constant and equal for the liquid and solid phases, T is related to the average volumic enthalpy H by the following equation:

$$H = c_p (T - T_0) + g_l \Delta H_{ls} \tag{8}$$

where ΔH_{ls} is the latent heat of fusion. Eq. (7) is a non-linear equation in enthalpy. Thus this equation is solved using a Newton–Raphson scheme with a Euler-backward time discretization.

2.3. Solute mass conservation equation

The present model of binary alloy solidification assumes that the phase diagram is linearized (constant liquidus slope and constant partition coefficient). At the scale of the microstructure, the solid and liquid phases are assumed to be at thermodynamic equilibrium (lever rule), which yields the equilibrium relations:

$$c_s^* = k_p c_l^* \tag{9}$$

$$T = T_{ls} + m c_l^* \tag{10}$$

where T_{ls} is the melting temperature of the pure substance and m the liquidus slope. The superscript $*$ denotes a value taken at the liquid–solid interface. Using the lever rule assumption, the mean concentration c can be expressed by:

$$c = g_s c_s + g_l c_l = \big(k_p + (1 - k_p) g_l\big) c_l \tag{11}$$

where k_p is the partition coefficient.

At the macroscopic scale, neglecting the diffusion of solute at this scale, the solute mass balance is governed by the equation:

$$\frac{\partial c}{\partial t} + \mathbf{V} \cdot \nabla c_l = 0 \tag{12}$$

The solute diffusion is negligible but necessary for numerical purposes. For this reason the diffusion term is expressed in terms of c and not in term of c_l.

$$\frac{\partial c}{\partial t} + \mathbf{V} \cdot \nabla c_l = \nabla \cdot (D_c \nabla c) \tag{13}$$

where D_c is the solutal diffusivity. Following Voller et al. [7], Eq. (13) is discretised in time as:

$$\frac{c - c^0}{\Delta t} + \mathbf{V} \cdot \nabla c - \nabla \cdot (D_c \nabla c) = \mathbf{V} \cdot \nabla \big(c^0 - c_l^0\big) \tag{14}$$

where c^0 denotes the solute content at the beginning of the time increment. The weak forms of Eqs. (7) and (13) are solved using the well-known Streamline Upwind/Petrov–Galerkin finite element method [11], with linear tetrahedral elements.

2.4. Solution strategy

The solution is based on a sequential staggered scheme. Eqs. (4), (5), (7), (13) are solved one time per time step. During a time increment, the solution procedure is composed of six steps:

(i) Solution of the energy conservation equation (7) (possibly time step optimization), output H;
(ii) Solution of the solute conservation equation (13), output c;
(iii) Calculation of g_l, T, c_l with the microsegregation model (Eqs. (8)–(11)). This is made locally, at each node, using the latest calculated values of c and H provided by steps (i) and (ii);
(iv) Solution of the mass and momentum conservation equations (Eqs. (4), (5)), output P, $\mathbf{V}$;
(v) Remeshing (if necessary);
(vi) Transport and updating of variables.

3. Adaptive anisotropic remeshing

3.1. Remeshing steps

The application of an adaptive anisotropic remeshing strategy can be divided in four steps:

(i) Calculation of the objective mesh size in the main mesh direction;
(ii) Calculation of the anisotropy coefficient to control the stretching of the elements;
(iii) Generation of the local metric matrix at each node;
(iv) Generation of a new mesh complying with the local metric (done by an external software, MTC [12]).

3.2. Metric definition

A metric M is represented by a symmetric, definite positive (3, 3) matrix (for a 3D case), which is used to calculate scalar products and hence distances. Given a vector u, the norm of u according to the metric M is defined by:

$$\|u\|_M = \sqrt{u^T \cdot M \cdot u} \tag{15}$$

So when using a locally defined metric M (varying with spatial coordinates), the distance between two points is dependent on their position. This allows a control of the mesh size in the different spatial directions because the mesher tries to obtain a uniform mesh (using the metric to calculate the size of the elements). The generation of the local metric at each node is performed in two steps: first an objective mesh size h is computed and then the orientation and the elongation of the new mesh are calculated. Then the metric matrix is build:

$$M = R^T \cdot \begin{pmatrix} \frac{1}{h^2} & 0 & 0 \\ 0 & \frac{1}{(\text{coef}\cdot h)^2} & 0 \\ 0 & 0 & \frac{1}{(\text{coef}\cdot h)^2} \end{pmatrix} \cdot R \tag{16}$$

where R is the rotation matrix defined by the main direction vector and two perpendicular vectors, coef is the value of the elongation ratio.

3.3. Objective mesh size

A main direction is defined locally. The direction of a gradient or of the velocity of the liquid is used to determine it. The procedure is described in the next section. The objective mesh size is the size of the element in the main direction prescribed by the adaptation procedure. The local mesh size is determined by three criteria for mushy and liquid areas:

- gradient of liquid fraction, $\|\nabla g_l\|$;
- gradient of mean concentration, $\|\nabla c\|$;
- gradient of the velocity norm, $\|\nabla\|\mathbf{V}\|\|$.

For each of these gradients, two threshold values and two corresponding mesh sizes are defined. The objective mesh size and the elongation factor are linearly integrated (see Fig. 1).

The objective mesh size is the minimum of the three values obtained using the three different criteria. The treatment of the solid part is quite different because of the hypothesis of no solid motion and no macro-diffusion of the solute in the solid. So in the solid part, the concentration field does not change. The remeshing of this part should only keep the information obtained by the calculation. Therefore, only the criterion based on the gradient of the mean concentration is considered. $h^{\text{obj}} = \frac{\Delta c^{\text{obj}}}{\|\nabla c\|}$ where Δc^{obj} is the objective mean concentration gap between two nodes of an element. This value is also bounded by a maximum and a minimal value. Using this strategy we obtain an objective mesh size at each node that combines the information coming from the solution of energy, solute and momentum equations.

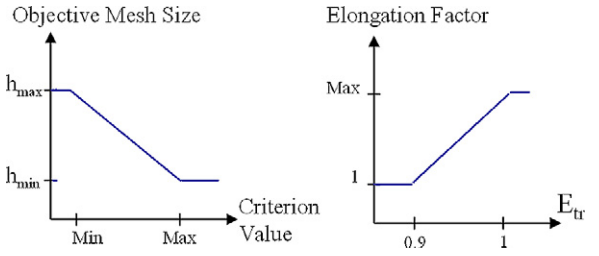

Fig. 1. Mesh size evolution with the criterion and elongation factor versus E_{tr} value.

Fig. 1. Taille de maille en fonction du critère sélectionné et facteur d'élongation en fonction de l'étirement, E_{tr}.

3.4. Anisotropy factors

The local anisotropy factors are the orientation of the mesh and the elongation factor. The first controls the direction in which the objective mesh size is applied and the second determines the objective mesh size in the two other directions. The calculation of the anisotropy is independent of the mesh size calculation, so different criteria are applied. The domain is divided in three different areas:

- the solid zone, controlled by the mean concentration gradient;
- the mushy zone, controlled by the liquid fraction gradient;
- the liquid zone, controlled by the velocity.

In each zone the main mesh direction is given by the unitary vector collinear to the relevant vector (e.g. the velocity vector in liquid zone). Then, the elongation factor is calculated using the change in direction of these vectors in an element following this formula:

$$E_{\text{tr}} = \max_{k=1,4} \left(\frac{\mathbf{V}_k \cdot \mathbf{V}_{\text{center}}}{\|\mathbf{V}_k\| \|\mathbf{V}_{\text{center}}\|} \right) \tag{17}$$

where k denotes the local node numbering and $\mathbf{V}_{\text{center}}$ denotes the velocity at the center of the element. After calculating the elongation factor, according to Fig. 1, the objective mesh size is multiplied by the elongation factor in the directions perpendicular to the mesh direction. On the other hand, in the liquid zone, the elongation factor is applied in the direction of the velocity. The metric is built using all these elements and sent to the remesher MTC, which will optimize the mesh topology using the local metric matrix.

3.5. Automatic control of the number of elements

Currently the remeshing is applied periodically; this period is fixed by the user. However, to avoid a huge increase of the number of elements, a control function has been added. After each remeshing we estimate the new correction factor and the corrected mesh size as followed:

$$f_{\text{corr}}^{\text{new}} = \left(\frac{n_{\text{elt}}}{n_{\text{elt}}^{\text{obj}}} \right)^{1/3} \cdot f_{\text{corr}}^{\text{old}} \quad \text{and} \quad h_{\text{obj}}^{\text{corr}} = f_{\text{corr}}^{\text{new}} \cdot h_{\text{obj}} \tag{18}$$

where n_{elt} is the current number of elements and $n_{\text{elt}}^{\text{obj}}$ the objective number of elements prescribed by the user. So the minimum mesh size evolves during the calculation as illustrated in the second application case, resulting in a number of elements maintained approximately constant. The minimum mesh size is reduced because the refined areas are growing due to the increasing complexity of the flow and the enlargement of the mushy zone and the corresponding boundary layer.

4. Applications

Two cases are presented in this section. For these two cases, a pseudo-2D approach has been used to shorten the calculation time. In this approach we consider that this is a plane case, and we impose two symmetry planes and use only one element in the thickness direction. Moreover, for the first case a full 3D computation has been performed.

4.1. Pb-48wt%Sn ingot

The application case consists of the solidification of a Pb-48wt%Sn ingot studied by Hebditch and Hunt [13]. In this test, the alloy is solidified in a parallelepipedic cavity (Fig. 2). The position of the horizontal sections used for experimental measurements is also indicated. The material properties and boundary conditions are presented in Table 1. This case has been used in a previous study to compare 2D and 3D macrosegregation codes with experimental data [9,14]. Four simulations have been performed: one with SOLID a FV code and three with THERCAST: two pseudo-2D with and without remeshing and one in 3D without adaptive remeshing. For computation time reasons,

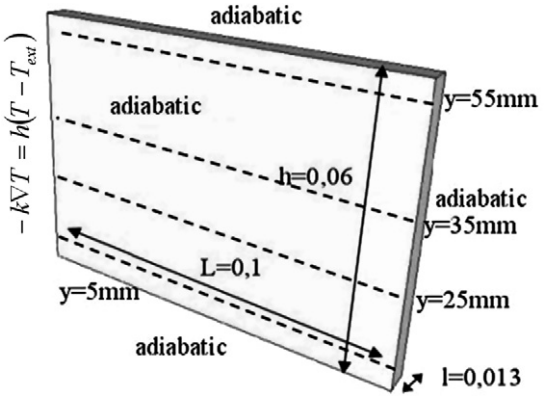

Fig. 2. Hebditch–Hunt case geometry.

Fig. 2. Géométrie du cas test Hebditch–Hunt.

Table 1
Material properties and physical parameters for the Pb-48wt%Sn ingot

Tableau 1
Propriétés du matériau et paramètres physiques pour le lingot utilisant l'alliage Pb-48wt%Sn

Thermal conductivity k	50 W m^{-1} K^{-1}	Initial temperature T_{init}	216 °C
Specific heat c_p	200 J kg^{-1} K^{-1}	Initial concentration c_0	48 wt%
Latent heat of fusion ΔH_{ls}	53.5 kJ kg^{-1}	Reference density ρ_0	9000 kg m^{-3}
Melting temperature T_{ls}	327.5 °C	Dynamic viscosity μ	10^{-3} Pa s
Liquidus line slope m	−2.3 K (wt%)$^{-1}$	Dendrite arm spacing λ_2	40 µm
Partition coefficient k_p	0.307	Heat convection coefficient h	400 W m^{-2} K^{-1}
Eutectic temperature T_{eut}	183 °C	Thermal expansion coefficient β_T	10^{-4} K^{-1}
External temperature T_{ext}	25 °C	Solutal expansion coefficient β_T	4.5×10^{-3} (wt%)$^{-1}$
		Solutal diffusivity D_c	10^{-9} m^2 s^{-1}

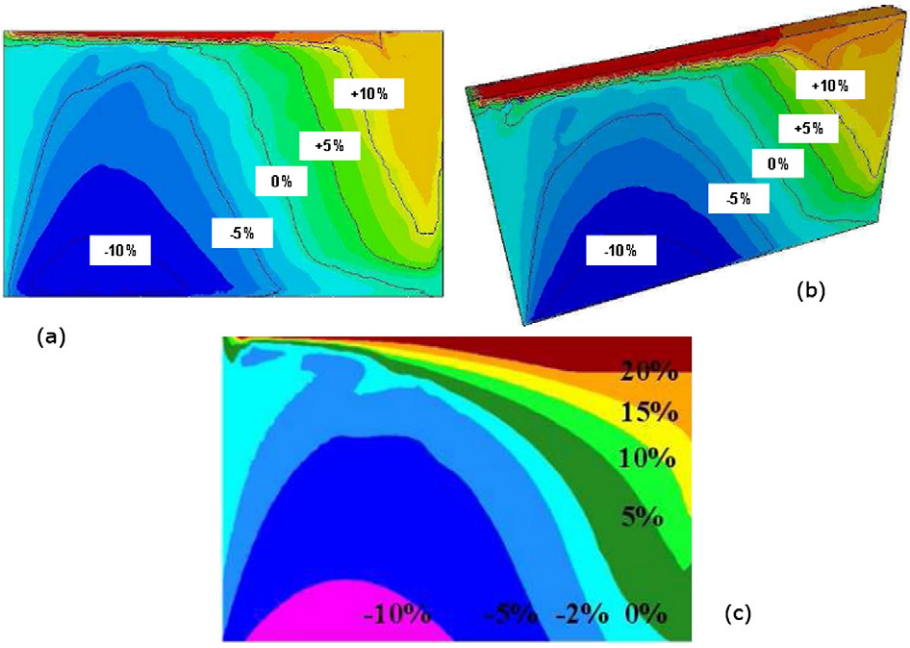

Fig. 3. Segregation pattern—comparison between THERCAST 2D (a) and 3D (b) and SOLID (c) after 400 s of solidification.

Fig. 3. Niveaux de ségrégation—comparaison entre THERCAST 2D (a) et 3D (b) ainsi qu'avec SOLID (c) après 400 s de solidification.

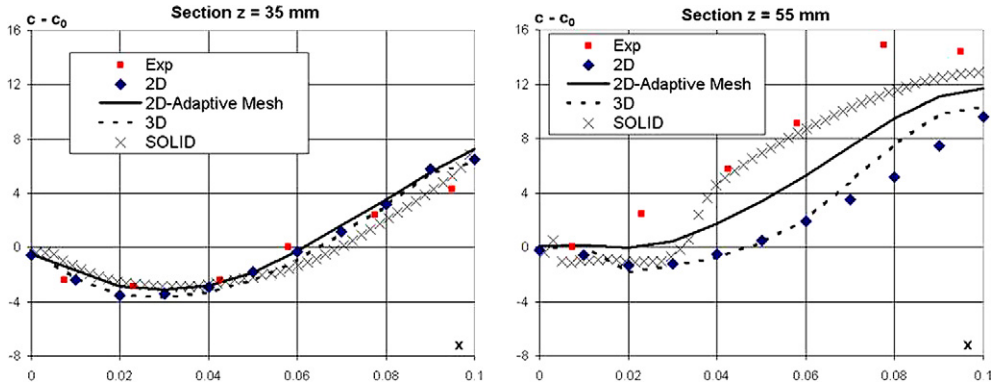

Fig. 4. Macrosegregation on horizontal section at the end of the solidification—effect of the 3D geometry and the adaptive remeshing.

Fig. 4. Macroségrégation sur deux sections horizontales à la fin de la solidification—effet de la géométrie 3D et du maillage adaptatif.

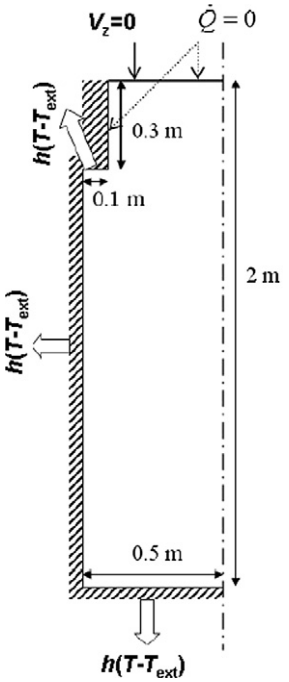

Fig. 5. Geometry of the steel ingot and boundary conditions.

Fig. 5. Géométrie du lingot en acier et conditions aux limites.

the full 3D simulation with adaptive remeshing has not been done. The segregation pattern at 400 s for the different simulations except for the pseudo-2D with remeshing are presented on Fig. 3. One can notice that the global shape of the iso-concentrations in tin are similar. The shape of the iso-concentrations in the upper left corner denotes that a channel has been formed in this region. It is interesting to recall that such a channel has not been found in the 2D study [14] with the finite element simulation. Only two significant sections are presented in Fig. 4. On this figure, the experimental data, the SOLID results and the pseudo-2D THERCAST results, with and without adaptive remeshing and the 3D THERCAST results are presented. The results of SOLID and THERCAST are in good agreement for the 35 mm-section with the experiment. However, on the 55 mm-section, significant differences appear. SOLID results show greater positive segregation and a small negative zone, with a rapid change between these two zones. For THERCAST, the segregation is globally lower, and the curves are smooth. In the case of the pseudo-2D computations, the effect of remeshing only appears in this 55 mm-section where we observe a huge change in the concentration. The

improvement of the results, in the sense that they are closer to the experimental results and to SOLID results, is highly visible even if the number of elements has not changed. So the adaptive remeshing seems reliable and efficient. The diminution of the segregation intensity in the upper section in the case of the 3D computation can be attributed to the damping effect of the vertical sides of the cavity on the flow field. This effect is only tackled in this 3D computation.

4.2. Steel ingot

The second application consists of a larger steel ingot (2 m height and 1 m width) without moulds and with insulation at the top of the domain as presented in Fig. 5. The alloy is a Fe-0.38wt%C. Its characteristics and the other parameters are listed in Table 2. Fig. 6 presents the result at 100 s: at that time a first layer of solid has formed on all the cooling surfaces. The flow field is well developed and a boundary layer appears near the solidification front. We can notice that the mesh is much coarser in the liquid bulk than in the mushy zone. However, on the mesh zoom, a refined zone appears also in the liquid where the gradient of velocity is very high. This corresponds to the boundary layer which is well captured by the remeshing technique despite its thickness which is small with regard to the size of the casting. The last two data presented are the mesh size and the E_{tr} value. The second indicates the areas where the mesh becomes isotropic (blue part are isotropic and red anisotropic, the elongation ration going from 1

Table 2
Material properties and physical parameters for the steel ingot

Tableau 2
Propriétés du matériau et paramètres physiques pour le lingot en acier

Reference density ρ_0	7060 kg m^{-3}	Initial temperature T_{init}	1528 °C
Dynamic viscosity μ	4.2×10^{-3} Pa s	Initial concentration c_0	0.38 wt%
Thermal conductivity k	30 W m^{-1} K^{-1}	Dendrite arm spacing λ_2	100 µm
Specific heat c_p	500 J kg^{-1} K^{-1}	Thermal expansion coefficient β_T	8.85×10^{-5} K^{-1}
Latent heat of fusion ΔH_{ls}	30.9 kJ kg^{-1}	Solutal expansion coefficient β_T	4.16×10^{-2} (wt%)$^{-1}$
Melting temperature T_{ls}	1538 °C	Solutal diffusivity D_c	10^{-9} m^2 s^{-1}
Liquidus line slope m	−80 K (wt%)$^{-1}$	Heat convection coefficient h	500 W m^{-2} K^{-1}
Partition coefficient k_p	0.18	External temperature T_{ext}	200 °C

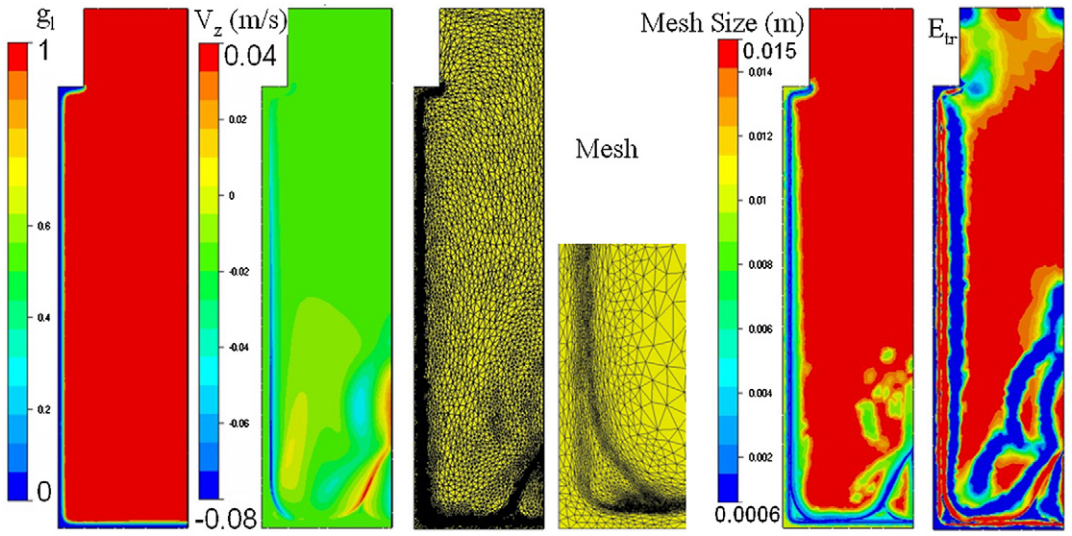

Fig. 6. Liquid fraction, vertical velocity, mesh and zoom on the left bottom corner, mesh size and E_{tr} values (blue indicates isotropic area (elongation ration = 1) and red indicates completely anisotropic area (elongation ratio = 4)) for the steel ingot at 100 s.

Fig. 6. Fraction de liquide, vitesse verticale, maillage avec un zoom sur le coin en bas à gauche, taille de maille et valeur de l'étirement E_{tr} (le bleu correspond aux zones isotropes (facteur d'élongation = 1) et le rouge correspond aux zones fortement anisotropes (facteur d'élongation = 4)) pour le lingot en acier à 100 s.

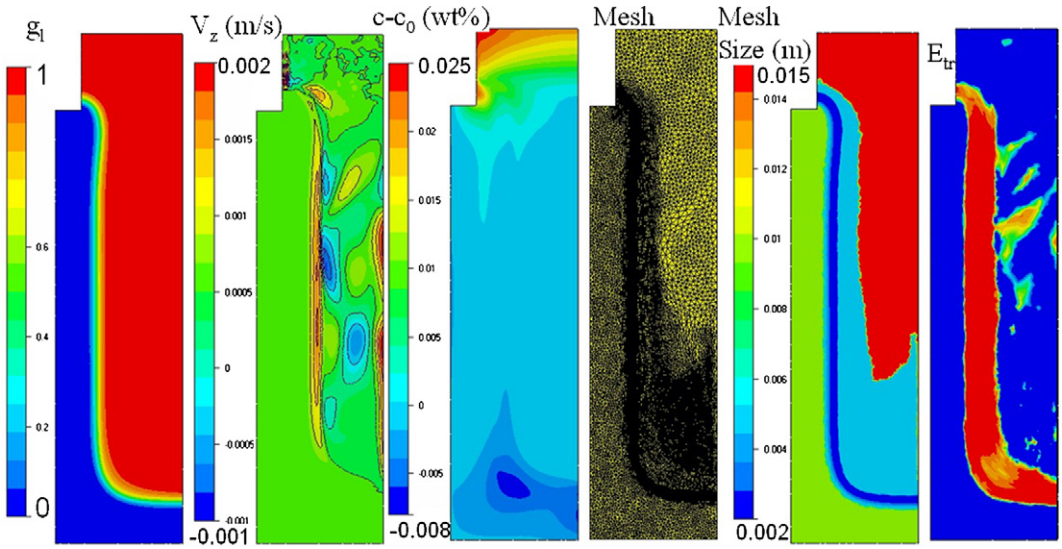

Fig. 7. Liquid fraction, vertical velocity, segregation, mesh, mesh size and E_{tr} values for the steel ingot at 2000 s.

Fig. 7. Fraction de liquide, vitesse verticale, ségrégation, maille, taille de maille et valeur de l'étirement E_{tr} pour le lingot en acier à 2000 s.

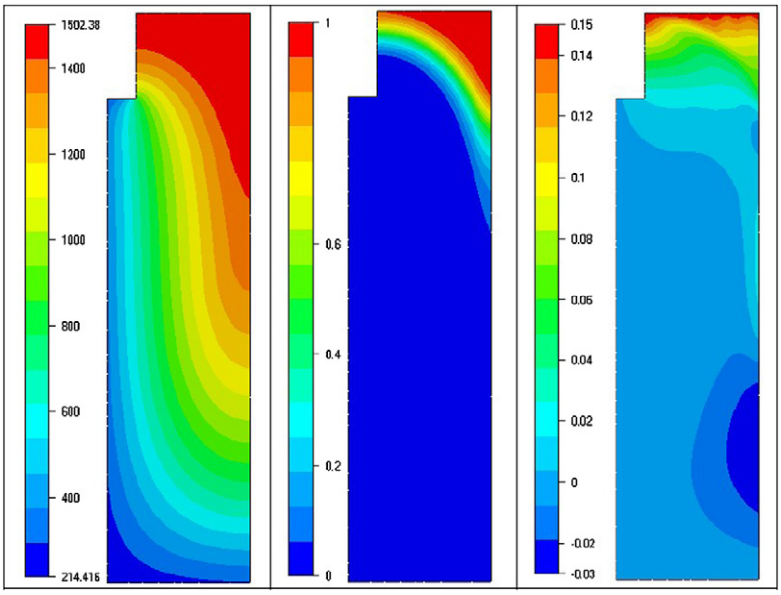

Fig. 8. Temperature, liquid fraction and segregation after 14 000 s.

Fig. 8. Température, fraction de liquide et ségrégation à 14 000 s.

to 4) due to the direction change of the velocity, for example. One can see that the mesh is globally anisotropic. On the other hand on Fig. 7, after 2000 s of solidification, the flow field is more complex with different recirculation areas. As a consequence, the mesh becomes isotropic in the liquid bulk. Moreover the mesh is isotropic in the solid part, and globally it tends to be more isotropic. This leads to a higher minimum mesh size (0.0006 m $\rightarrow$ 0.002 m) to keep constant the number of elements. At 2000 s the macrosegregation in the ingot is also significant, and we can see that it is mainly concentrated in the feeder. The final segregation pattern in C is presented on Fig. 8, a negative macrosegregation is predicted at the bottom of the ingot and a positive at the top. This is in good agreement with the observations on this type of product. This example shows the feasibility of macrosegregation simulation on large ingot using anisotropic mesh adaptation.

5. Conclusions

An anisotropic mesh adaptation strategy has been implemented in the 3D FEM code THERCAST in order to predict macrosegregation. This strategy has been applied on a reference case and has demonstrated a clear improvement. A feasibility study has shown promising results on a large steel ingot.

Acknowledgements

This work has been supported by the French Ministry of Industry, the French Technical Center of Casting Industries (CTIF) and the companies Arcelor, Ascometal, Aubert et Duval, Erasteel, Industeel Creusot and PSA.

References

[1] J.-L. Desbiolles, Ph. Thevoz, M. Rappaz, Micro-/macrosegregation modeling in casting: a fully coupled 3D model, in: Proceedings of Modeling of Casting, Welding and Advanced Solidification Processes X, TMS, 2003, pp. 245–252.
[2] G. Quillet, A. Ciobanas, P. Lehmann, Y. Delannay, M. Medina, Y. Fautrelle, Modelling of the mesosegregations in a binary alloy under the influence of a forced convection, in: Proceedings of Modeling of Casting, Welding and Advanced Solidification Processes X, TMS, 2003, pp. 253–260.
[3] O. Jaouen, 1998, Modélisation tridimensionnelle par éléments finis pour l'analyse thermo-mécanique du refroidissement des pièces coulées, PhD Thesis, Ecole des Mines de Paris.
[4] J. Ni, C. Beckermann, A volume-averaged two-phase model for transport phenomena during solidification, Metall. Trans. B 22 (1991) 349–361.
[5] W.D. Bennon, F.P. Incropera, A continuum model for momentum, heat and species transport in binary solid–liquid phase change systems—I. Model formulation, Int. J. Heat Mass Transfer 30 (1987) 2161–2170.
[6] Y. Fautrelle, P. Lehmann, G. Quillet, M. Medina, F. Durand, Y. du Terrail, Modelling of the meso-segregations under the influence of forced convection: a statistical phase-averaged approach, in: P. Ehrard, D. Riley, P.H. Steen (Eds.), Interactive Dynamics of Convection and Solidification, Kluwer Academic, Dordrecht/London, 2001, pp. 87–97.
[7] V.R. Voller, A.D. Brent, C. Prakash, The modelling of heat, mass and solute transport in solidification systems, Int. J. Heat Mass Transfer 32 (1989) 1719–1731.
[8] M.C. Schneider, C. Beckermann, A numerical study of the combined effects of microsegregation, mushy zone permeability, and contraction driven flow on macrosegregation and eutectic formation in binary alloy solidification, Int. J. Heat Mass Transfer 38 (1995) 3455–3473.
[9] S. Gouttebroze, V. Fachinotti, M. Bellet, H. Combeau, 3D-FEM modeling of macrosegregation in solidification of binary alloys, in: Proceedings of Seventh ESAFORM Conference, Trondheim, 2004, pp. 421–424.
[10] T.E. Tezduyar, Y. Osawa, Finite element stabilization parameters computed from element matrices and vectors, Comput. Methods Appl. Mech. Engrg. 190 (2000) 411–430.
[11] A.N. Brooks, T.J.R. Hughes, Streamline upwind/Petrov–Galerkin formulations for convection dominated flows with particular emphasis on the incompressible Navier–Stokes equations, Comput. Methods Appl. Mech. Engrg. 32 (1982) 199–259.
[12] T. Coupez, H. Digonnet, R. Ducloux, Parallel meshing and remeshing, Appl. Math. Model. 25 (2) (2000) 153–175.
[13] D.J. Hebditch, J.D. Hunt, Observations of ingot macrosegregation on model systems, Metall. Trans. 5 (1974) 1557–1564.
[14] N. Ahmad, H. Combeau, J.-L. Desbiolles, T. Jalanti, G. Lesoult, M. Rappaz, C. Stomp, Numerical simulation of macrosegregation: A comparison between finite volume method and finite element method predictions and a confrontation with experiments, Metall. Mater. Trans. 29A (1997) 617–630.